Bioactive Materials 6 (2021) 602–612

Contents lists available at ScienceDirect

Bioactive Materials

journal homepage: http://www.keaipublishing.com/biomat

Galvanic replacement reaction for in situ fabrication of litchi-shaped heterogeneous liquid metal-Au nano-composite for radio-photothermal cancer therapy

Zhenhu Guo[a,b,c], Jingsong Lu[b,c,d], Dan Wang[b,c,e], Wensheng Xie[b,c,f], Yongjie Chi[b,c,g], Jianzhong Xu[b,c], Nonaka Takuya[b,c], Junxin Zhang[b,c], Wanling Xu[b,c], Fei Gao[h], Hong Wu[a,**], Lingyun Zhao[b,c,*]

[a] State Key Laboratory of Powder Metallurgy, Powder Metallurgy Research Institute, Central South University, Changsha, Hunan, 410083, China
[b] Key Laboratory of Advanced Materials, Ministry of Education of China, School of Materials Science and Engineering, Tsinghua University, Beijing, 100084, China
[c] State Key Laboratory of New Ceramics and Fine Processing, School of Materials Science and Engineering, Tsinghua University, Beijing, 100084, China
[d] Research Center of Magnetic and Electronic Materials, College of Materials Science and Engineering, Zhejiang University of Technology, Hangzhou, Zhejiang, 310014, China
[e] Department of Nanoengineering, Chemical Engineering Program, and Moores Cancer Center, University of California San Diego, La Jolla, CA, 92093, United States
[f] The Key Laboratory of Bioorganic Phosphorus Chemistry & Chemical Biology (Ministry of Education), Department of Chemistry, Tsinghua University, Beijing, 100084, China
[g] School of Earth Sciences and Resources, China University of Geosciences (Beijing), Beijing, 100083, China
[h] Shaanxi University of Chinese Medicine, Xi'an, Shanxi, 712046, China

ARTICLE INFO

Keywords:
Au nanodots
Gallium
Galvanic replacement reaction
Indium
Radio-photothermal therapy

ABSTRACT

With tremendous research advances in biomedical application, liquid metals (LM) also offer fantastic chemistry for synthesis of novel nano-composites. Herein, as a pioneering trial, litchi-shaped heterogeneous eutectic gallium indium-Au nanoparticles (EGaIn-Au NPs), served as effective radiosensitizer and photothermal agent for radio-photothermal cancer therapy, have been successfully prepared using in situ interfacial galvanic replacement reaction. The enhanced photothermal conversion efficiency and boosted radio-sensitization effect could be achieved with the reduction of Au nanodots onto the eutectic gallium indium (EGaIn) NPs surface. Most importantly, the growth of tumor could be effectively inhibited under the combined radio-photothermal therapy mediated by EGaIn-Au NPs. Inspired by this approach, in situ interfacial galvanic replacement reaction may open a novel strategy to fabricate LM-based nano-composite with advanced multi-functionalities.

1. Introduction

Rapid progress on the biomedical application of liquid metals (LM) has witnessed the tremendous research advance of these novel functional materials [1–5]. Simultaneously owning multi-properties such as high fluidity, excellent thermal and electrical conductivities, ideal biocompatibility, good radiopacity, controllable behaviors and conformability associated with reversible liquid-solid phase transition, facile manufacture and along with affordable cost, LM biomaterials have been widely applied in biological imaging [6,7], bone repair [8], drug delivery [9–11], magnetic hyperthermia [12,13], photothermal therapy [14–16], tumor embolotherapy [17], microwave dynamic therapy and microwave thermal therapy [18]. Such 'One material, Multi-functionalities' is rather unusual among many existing top materials and therefore it is noteworthy to recognize that a new direction of biomedical category: the LM biomaterials have formed [2].

Except for the diverse biomedical applications related to the unique properties of LM having been explored, meanwhile, extraordinary phenomena and characteristics with LM also attain unusual interests. Such novel findings may further offer platform as chemical reaction media to facilitate the synthesis of new functional materials. In 2016, for the first trial, the galvanic replacement reaction has been achieved

Peer review under responsibility of KeAi Communications Co., Ltd.
* Corresponding author. Key Laboratory of Advanced Materials, Ministry of Education of China, School of Materials Science and Engineering, Tsinghua University, Beijing, 100084, China.
** Corresponding author.
E-mail addresses: wuhong927@126.com (H. Wu), lyzhao@mail.tsinghua.edu.cn (L. Zhao).

https://doi.org/10.1016/j.bioactmat.2020.08.033
Received 15 June 2020; Received in revised form 6 August 2020; Accepted 15 August 2020

on LM Galinstan [19]. Anthony Mullane et al. successfully extended the galvanic replacement on Galinstan both on the bulk scale to generate LM core/solid metal shell marbles, and on the nanoscale to form nanorice particles for catalytic purpose [19]. Furthermore, it has been revealed that LM would normally undergo self-limiting Cabrera-Mott oxidation in the air and easily form atomically thin planar metallic compounds with minimum grain boundaries [20,21]. Such phenomenon has been recently exploited for the fabrication of a variety of novel 2D materials based on interfacial reactions for the application in microfluidics [22], wearable devices [23] and self-repairing flexible electronics [24,25], etc. More importantly, by sonication, microchannels or grinding protocols [26–28], LM nanoparticles (NPs), which possessing own advantages as compared with bulky form, could be prepared and have found such diverse applications in antitumor therapy [29,30], antibacterial [31], soft electronics [32] and thermal management field [33]. Putting the above-mentioned properties together, i.e. interfacial reactions by surface oxidation combined with galvanic replacement reactions with oxidation skin coating on each LM NPs, in situ fabrications of nano-heterogeneous core-shell structure could be achieved. Therefore, rather than a novel kind of functional materials with fundamental interest, the unprecedented chemistry offered by LM may also provide facile manner that has significant implications for many applications as well. Most recently, the growth of MnO_2 and Ag nanosheets on the LM NPs had been achieved by the reduction of the permanganate ions and $AgNO_3$ solution [34,35]. The as-prepared nano-heterogeneous structures could be successfully applied as efficient photocatalysis or real-time self-repairing flexible circuit materials. However, to date, no attempt has been made to apply such protocol in LM based nano-composite for biomedical application, given the rapid progress of LM composite for diverse applications in biomedicine. In this work, envisaged by the interfacial galvanic replacement reaction on the nano-LM for the synthesis of hybrid structure, as the first trial, we successfully fabricated the litchi-shaped heterogeneous eutectic gallium indium-Au (EGaIn-Au) nano-composite for anti-tumor treatment.

With high-atomic number and chemical inertness, Au has showed a great potential as radiosensitizer and photothermal agent due to its advantages with large photoelectric absorption coefficient and near-infrared (NIR) absorption ability [36–38]. Nano-formulations of EGaIn LM also have been proved to be effective in cancer theranostics. Therefore, it would be wise to combine these two components into one nano-hybrid platform by virtue of the interfacial galvanic replacement reactions offered by LM. In our previous demonstration, the EGaIn alloy displays magnetic field-driven thermochemotherapy and dual stimuli-responsive drug for cancer theranostics [13]. Here, we discovered that the EGaIn-Au nano-composite could effectively response to X-ray and NIR laser irradiation, which endowed the nano-composite with photothermal conversion ability and radiosensitization effect to kill cancer cells and achieve excellent therapeutic effect. Most importantly, the negligible tissues damage and significant limitation on growth of tumor tissues after NIR laser and X-ray treatment revealed the potential biomedical application of combined photothermal therapy and radiotherapy based on litchi-shaped heterogeneous EGaIn-Au nano-composites for cancer disease (Scheme 1).

2. Materials and methods

2.1. Materials

Eutectic gallium indium (Ga:In = 75 : 25 wt %, 6.35 g/cm^3) bulk liquid metal was purchased from Wochang Metal Products Co., Ltd (Dongguan, China). Xanthan gum, gelatin and $HAuCl_4{\cdot}3H_2O$ (≥99.9%) powder were provided by Aladdin Biochemical Technology (Shanghai, China) and Sinopharm Chemical Reagent Co., Ltd (Shanghai, China), respectively. High-glucose dulbecco's modified eagle's medium (H-DMEM), RPMI 1640 medium (RPMI 1640), penicillinstreptomycin (PS), fetal bovine serum (FBS), trypsin, bovine serum albumin (BSA), Cell Counting Kit-8 (CCK-8), Calcein-AM and propidium iodide (PI) were supplied by Biotopped Life Sciences (Beijing, China).

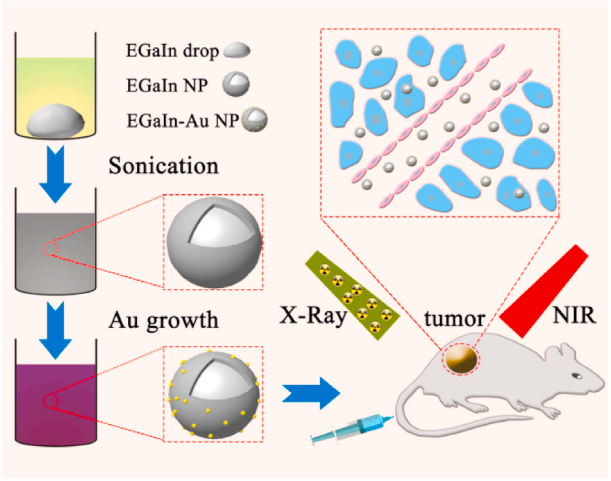

Scheme 1. Illustration of litchi-shaped heterogeneous EGaIn-Au nano-composites in preparation and application for radio-photothermal tumor therapy.

2.2. Instruments

The morphology of the samples was measured by transmission electron microscopy (HT-7700, Hitachi, Japan) and scanning electron microscope (S-4800, Hitachi, Japan). Energy-dispersive X-ray spectroscopy elemental mapping was collected by high-resolution transmission electron microscopy (JEM, JEOL, Japan). Photothermal effect was tested via an irradiation of 808 nm laser (GSCLS-05-7W00, Daheng Group Inc., China) and monitored by an ultrafine thermocouple fiber (ThermAgile-RD, Xi'an Heqi Opto-Electronic Technology Co., Ltd., China) and thermal imaging camera (F226S/B3S, FOTRIC, USA). Absorbance curve was measured by microplate reader (Varioskan LUX, Thermo Fisher Scientific Inc. Waltham, Massachusetts, USA). Element concentration was obtained from inductively coupled plasma-optical emission spectroscopy (Thermo Icap 6300, USA). Live/dead staining was obtained from the confocal laser scanning microscope (CLSM, Zeiss LSM 780, Germany) equipped with the Fluoview FV300 imaging software. The T_2-weighted MR images were collected by Philips 3.0 T whole-body MRI scanner (Achieva TX, Philips Medical System, Best, Netherlands).

2.3. Preparation and characterization of EGaIn-Au NPs

Before the preparation of EGaIn-Au nano-composite, the EGaIn NPs were synthesized via a typical probe-sonicating method. 200 μL of bulk EGaIn liquid metal was added into glass vial including 5 mL xanthan gum solution with 0.5% concentration. After ultra-sonication treatment for 5 min, the slurry was collected via centrifugation at 2000 rmp for 3 min and then re-suspended in DI water. The resulting spherical EGaIn NPs were washed to remove redundant xanthan gum and re-suspended in DI water. Afterward, 10 mL $HAuCl_4$ solution (20 mM) was added into EGaIn NPs suspension to trigger the in situ growth of Au NPs through interfacial galvanic replacement reactions. Finally the EGaIn-Au nano-composites were collected via a centrifugation and washed with DI water. For transmission electron microscopy characterization, the EGaIn-Au suspension was dropped on the lacey carbon transmission electron microscopy copper grid for observation.

2.4. Photothermal performance test

The photothermal heating effect of EGaIn NPs and EGaIn-Au nano-composite was investigated via 808 nm laser exposure of 0.5 mL of each

sample in 48-well plate with a continuous wave mode. In order to evaluate the effect of NPs concentration, samples with various concentrations including 500 μg/mL, 200 μg/mL, 100 μg/mL, 50 μg/mL were prepared and subject to NIR for 10 min at 1.5 W/cm^2. Meanwhile, the temperature-rise activity of EGaIn and EGaIn-Au composite with 0.5 W/cm^2, 1.0 W/cm^2, 1.5 W/cm^2, 2.0 W/cm^2 power densities at 200 μg/mL were also measured. In addition, the photothermal stability was tested via a cycling test in a 500 μg/mL concentration. Finally, the enhanced photothermal conversion efficiency was assessed by referring previous calculation method [14,39,40]. Details are as follows:

$$\eta = \frac{hS(T_{max} - T_{sur}) - Q_s}{I(1 - 10^{-A})} \quad (1)$$

where, h represents the heat transfer coefficient and S is the surface area of the container, T_{max} and T_{sur} mean the maximum temperature of samples (EGaIn NPs: 49.7 °C, EGaIn-Au NPs: 65.3 °C) under continuous laser irradiation (808 nm) and ambient temperature of surrounding (EGaIn NPs: 27.1 °C, EGaIn-Au NPs: 25.4 °C) respectively. Q_s represents the heat dissipation from the light absorbance by the solvent and the quartz sample cell which was calculated to be 0.0211 W. I means the laser irradiation power (1.5 W/cm^2) and A represents the absorbance of the sample under the excitation of laser which was recorded by microplate reader to be 0.517 for EGaIn NPs and 0.679 for EGaIn-Au NPs respectively.

H and s can be calculated via following equation:

$$hS = \frac{m_s C_s}{\tau_s} \quad (2)$$

M_s and C_s mean the mass and heat capacity of solvent which was 0.5 g and 4.2 J/g respectively. τ_s represents the sample system time constant that can be calculated from the linear curve fitting of temperature cooling time which was 317.24 for EGaIn NPs and 211.09 for EGaIn-Au NPs. The formula for calculation is as follows:

$$\tau_s = -\frac{t}{ln\theta} \quad (3)$$

where t means the change of temperature cooling time and the formula for θ is as follows:

$$\theta = \frac{T - T_{sur}}{T_{max} - T_{sur}} \quad (4)$$

where T-T_{sur} represents the change of temperature following the cooling time and T_{max}-T_{sur} represents the maximum change of temperature for surrounding temperature under continuous laser irradiation.

2.5. Cell culture

Mouse Fibroblast cells (L929 cell line) and mouse breast cells (4T1 cell line) were obtained from the American type culture collection and cultured in RPMI 1640 and H-DMEM complete medium including 89% basic medium, 10% FBS and 1% penicillin-streptomycin in an incubator at 37 °C under an atmosphere of 5% CO_2 and 90% relative humidity respectively. The cell passage was carried out using 0.25% (w: v) trypsin to digest adherent cells at a split ratio of 1:5 and then passages were cultured in new medium.

2.6. Gel dosimetry

According to a typical method [41,42], the gelatin (2.08 g) was added into DI water (19.57 mL) under stirring at 50 °C, and hydroquinone solution (0.04 g/mL, 1 mL) was then dropped into gelatin solution when the gelatin dissolved completely. Afterward, the methacrylic acid (1.5 mL), ascorbic acid (0.0075 g), and copper sulphate powder (0.005 g) were added into above mixture solution and stirred for 10 min. The obtained gel was used to disperse the EGaIn and EGaIn-Au nano-composite with 100 μg/mL concentration. Subsequently, the gel with different treatments was irradiated by X-ray and stored in no light environment for 2 days. Finally the gel was scanned by MRI to obtain the T_2-weighted MRI signal.

2.7. Clonogenic assay

The clonogenic assay was investigated to assess the radiosensitizer efficiency of EGaIn NPs and EGaIn-Au nano-composite by analyzing the survival fraction, a function of radiation dose. Mouse breast cells (4T1 cell line) were seeded in the 6-well at a density 2 × 10^4 per well and cultured for 24 h. Afterward, the medium was replaced with fresh H-DMEM completed medium with a 50 μg/mL concentration of EGaIn or EGaIn-Au composite respectively. When incubation for another 24 h, the 6-well plated was irradiated by X-ray at a dose of 0, 2, 4 Gy. After incubation for 10 days, the irradiated cells were washed with PBS solution and fixed by polyformaldehyde (4%). Subsequently, the cells were stained with trypan blue (0.4%) and then counted.

2.8. In vitro biocompatibility

For *in vitro* experiment, mouse fibroblast cells (L929 cell line) were seeded in the 96-well at a density 5000 per well for 24 h. Afterward, the original medium was replaced by RPMI 1640 complete medium containing EGaIn and EGaIn-Au composite with various concentrations 12.5 μg/mL, 25 μg/mL, 50 μg/mL, 100 μg/mL, 200 μg/mL. After 24 h and 48 h of in-culture, the CCK8 assay was used to assess the cell viability.

2.9. In vitro cytotoxicity

Mouse breast cells (4T1 cell line) were seeded in the 96-well at a density 5000 per well. After 24 h, the original medium was removed and the cells were cultured with EGaIn and EGaIn-Au composite solution with concentration of 100 μg/mL. Afterward, the 96-well plate was irradiated by 808 nm laser with different power density 1.0 W/cm^2, 1.5 W/cm^2, 2.0 W/cm^2. Finally, the cell viability was assessed via CCK8 assay.

2.10. In vivo long-term toxicity study

All animal experiments were performed according to the guidelines by the Institutional Animal Care and Use Committee (IACUC) of Tsinghua University. The 6-week female BALB/c mice were divided into four groups (5 mice at each) randomly. And then the mice were injected with EGaIn-Au NPs with different dose (100 μL, 30 mg kg^{-1}, 60 mg kg^{-1}, 90 mg kg^{-1} and 120 mg kg^{-1}). The survival state and body weight of mice was recorded every day.

2.11. In vivo anticancer efficiency

BALB/c mice of 5 weeks were implanted with 4T1 tumor tissue to build tumor model *in vivo*. When the tumor volume reached about 50 mm^3, the mice were divided into five groups with various treatments: (1) intravenously injected with PBS (2) intravenously injected with EGaIn-Au composite only (3) intravenously injected with EGaIn-Au nano-composite + NIR treatment (4) intravenously injected with EGaIn-Au nano-composite + X-ray irradiation treatment (5) intravenously injected with EGaIn-Au nano-composite + X-ray irradiation + NIR treatment. After administration for 24 h, the mice were irradiated with 808 nm laser at 1.5 W/cm^2 for 10 min or X-ray alone. For EGaIn-Au composite + X-ray irradiation + NIR group, the mice were firstly irradiated by X-ray and then 808 nm laser. The tumor size and body weight were recorded every 2 days. The relative body weight was calculated as W/W_0 (W_0 was body weight when the injection was initiated) and the relative volume was calculated as V/V_0 (V_0

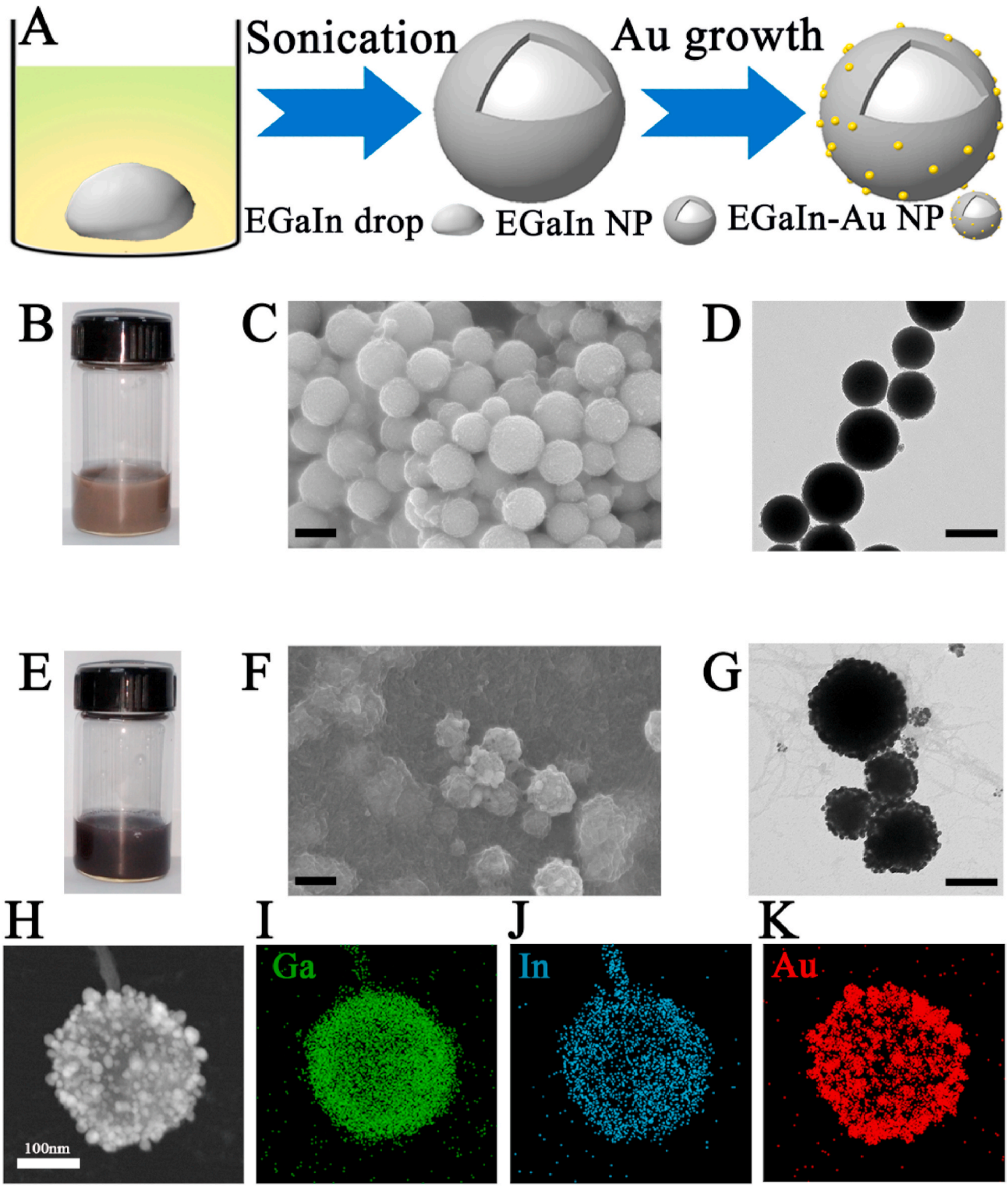

Fig. 1. (A) Schematic illustration of synthetic procedure of EGaIn NPs and EGaIn-Au nano-composite. (B) Photographs of as-synthesized EGaIn NPs suspension. (C) Representative scanning electron microscope (SEM) images of EGaIn NPs. Scale bars: 200 nm. (D) TEM images of as-synthesized spherical EGaIn NPs. Scale bar: 200 nm. (E) Photographs of EGaIn-Au nano-composite suspension. (F) Representative SEM images of EGaIn-Au NPs. Scale bars: 200 nm (G) TEM images of litchi-shaped heterogeneous EGaIn-Au nano-composite. Scale bar: 200 nm. (H) High-angle annular dark-field-scanning TEM and (I–K) element distribution of Au, Ga, In on EGaIn-Au composite surface.

was tumor volume when the injection was initiated). After 19 days, the mice were sacrificed and the major organs including heart, liver, spleen, lung, kidney and tumor tissue were collected to HE staining.

2.12. Statistical analysis

Statistical analysis was carried out using one-way ANOVA followed by a Newman – Keuls post hoc *t*-test with the SPSS (IBM7 SPSS Version

23) for windows. ** indicates P-values of < 0.01, *** indicates P-values of < 0.001. Both of them were considered to be statistically significantly.

3. Results and discussion

3.1. Synthesis and characterization of EGaIn-Au nano-composites

Before the preparation of EGaIn-Au NPs, the EGaIn NPs were prepared by ultra-sonication with xanthan gum as surfactant or stabilizer (Fig. 1A). After sonication treatment for bulk EGaIn, the EGaIn colloids with a grey color could be observed (Fig. 1B). As shown in scanning electron microscope (SEM) images (Fig. 1C) and transmission electron microscope (TEM) images (Fig. 1D), the as-prepared EGaIn NPs appeared as core-shell structured nanospheres which evenly coated with xanthan gum, a water-soluble natural exo-polysaccharide generated by gram-negative bacterium *Xanthomonas campestris* and widely applied as a suspending and thickening agent in food industry [43,44]. Herein, as the pioneering trial, we employed it as the surfactant in the preparation of LM NPs and its ideal stabilization effect for NPs formulation had been confirmed. After addition of $HAuCl_4$ solution, it could be noticed that the grey color gradually turned into violet (Fig. 1E), which indicating a reduction of Au ions and presence of Au NPs. This phenomenon was benefited from the interfacial galvanic replacement reaction contributed by Ga and Au ions [45–47]. SEM images (Fig. 1F) and TEM observations (Fig. 1G) depicted that EGaIn-Au nano-composite presented a litchi-shaped heterogeneous structure with diameter approximately 200 nm. Furthermore, high resolution transmission electron microscopy (HRTEM) images combined with energy dispersion spectrum (EDS) showed that Ga, In and Au were uniformly presented on the surface of EGaIn-Au nano-composite (Fig. S1 and Fig. 1H–K). In addition, HRTEM images combined with selected area electron diffraction (SAED) patterns obviously presented the presence of Au NPs on the surface of EGaIn-Au NPs (Fig. S2).

3.2. Photothermal performance of EGaIn-Au nano-composites

As a novel photothermal agent candidate in metal family, LMs have attracted a lot of significant attentions due to the ideal photothermal conversion efficiency [8,48]. With the reduction of Au NPs on the surface of EGaIn NPs, the comparison of photothermal conversion performance of pure EGaIn NPs and EGaIn-Au NPs was performed. Firstly, the UV–vis absorbance spectra of both samples were measured (Fig. S3A), in which the increased absorbance value of EGaIn-Au NPs suspension at NIR 808 nm indicated the contribution of reduced Au layer onto EGaIn NPs. Next, both samples with different concentrations were exposed under 808 nm laser for 10 min. As revealed by Fig. 2A and Fig. S3C, the temperature elevation curves monitored by optical fiber showed that both samples could rapidly and efficiently generate heat while under NIR exposure. Moreover, EGaIn-Au NPs presented an obvious enhancement for temperature increase under the same concentration as compared with that of pure EGaIn NPs. Furthermore, the photothermal effect was positively relevant to the irradiation power intensity (Fig. 2B and Fig. S3E), and Fig. S3B and Fig. S3D also demonstrated the observation by infrared thermal images. In addition, a reproducible temperature change patterns were observed for two cycles and the excellent thermal-stability of the two samples could be confirmed (Fig. S3F). The detailed information of photothermal performance was supplied in Fig. 2C–D and Figs. S3G–H, and on the basis of quantification method developed by Roper [40] the calculated photothermal conversion efficiency is 7% and 22.58% for EGaIn NPs and EGaIn-Au NPs respectively, which is comparable to some common photothermal agents such as metal material, semiconductor material, carbon material, organic material and enough for effective photothermal therapy [49,50]. In addition, TEM observation also suggested that the morphology of both samples would keep integrity after NIR exposure (Fig. 2E and Fig. S4). Currently, the disappointing stability (including the colloid, chemical and thermal stability) of the LM NPs has been noticed, which would impede the further application in cancer treatment [51,52]. In the current study, the application of xanthan gumas surfactant when preparing the EGaIn NPs would provide help to control the morphological and thermal stabilization.

3.3. Biocompatibility and cytotoxicity of EGaIn-Au nano-composites

Except for high photothermal conversion performance and superior photothermal stability, the ideal biocompatibility is also a critical criterion for being an excellent photothermal therapy agent. Murine fibroblast cell line L929 was employed for the *in vitro* cytotoxicity evaluation. Fig. 3A and Fig. 3B demonstrated that after co-incubation the cells with the both samples containing cultural medium, the cell viability remained above 80% at all NPs concentration (200 μg/mL, 100 μg/mL, 50 μg/mL, 25 μg/mL, 12.5 μg/mL), indicating the negligible cytotoxicity and ideal *in vitro* biocompatibility. Next, 4T1 murine breast cancer cell line was adopted to evaluate the photothermal performance mediated by both samples. After co-incubation for 24 h under 100 μg/mL concentration, the cells were treated with 808 nm laser irradiation at various power densities (2.0 W/cm^2, 1.5 W/cm^2, 1.0 W/cm^2, 0 W/cm^2) for 5 min. Cell activity without treatment kept healthy and the cell viability treated with EGaIn or EGaIn-Au NPs significantly declined after laser irradiation according to different power densities (Fig. 3C). It could be clearly noticed that EGaIn-Au NPs could induce a great photothermal effect and present a superior cancer cells killing ability to EGaIn NPs. Meanwhile, there was an obvious positive association between photothermal ablation ability and power density for two samples. Moreover, the calcein-AM and propidium iodide-fluorescent probe were used to stain cells, in which the living cells could be stained with green fluorescence and dead cells with red fluorescence (Fig. 3D). These results showed that the EGaIn-Au NPs could be used as a more effective heat mediator to convert light energy into heat energy for hyperthermia treatment of cancer cells.

3.4. Gel dosimetry and clonogenic assay

It is generally recognized that materials with high atomic numbers can effectively convert the X-ray radiation energy by means of excellent X-ray absorption coefficient to produce secondary electrons for radiosensitization [53,54]. The dose enhancement ability of radiosensitizer is a significant parameters to evaluate radiotherapy effect, which can be tested by gel dosimetry protocol [42]. In this study, the modified MAGIC gel dosimetry developed by Fong [55] was used to evaluate the dose enhancement contributed by both samples under different radiation densities. After irradiation, the gel containing 100 μg/mL EGaIn NPs or EGaIn-Au composite exhibited a different polymerization response, in which a negative T_2-weighted MRI signal enhancement (Fig. 4A) after MRI scanner could be clearly observed accompanied with a color change from transparent to white (Fig. 4B). Further on, the clonogenic assay was conducted to assess the radiosensitizer efficiency by testing the survival fraction of 4T1 cells at different radiation dose. As results shown in (Fig. 4C and D), the EGaIn-Au NPs presented an obvious chronic cytotoxicity than control group with X-ray alone and enhanced radiotherapy efficiency than EGaIn NPs group. So it can be confirmed that the radio-sensitization ability of EGaIn NPs could be obviously improved after in situ growth of Au NPs on surface via interfacial galvanic replacement reaction.

3.5. In vivo antitumor treatment

Inspired by the excellent photothermal conversion efficiency, high biocompatibility, effective tumor cells killing ability and *in-vitro* radio sensitivity property, we further investigated the *in vivo* radio-photothermal therapy for anti-cancer treatment mediated by the EGaIn-Au

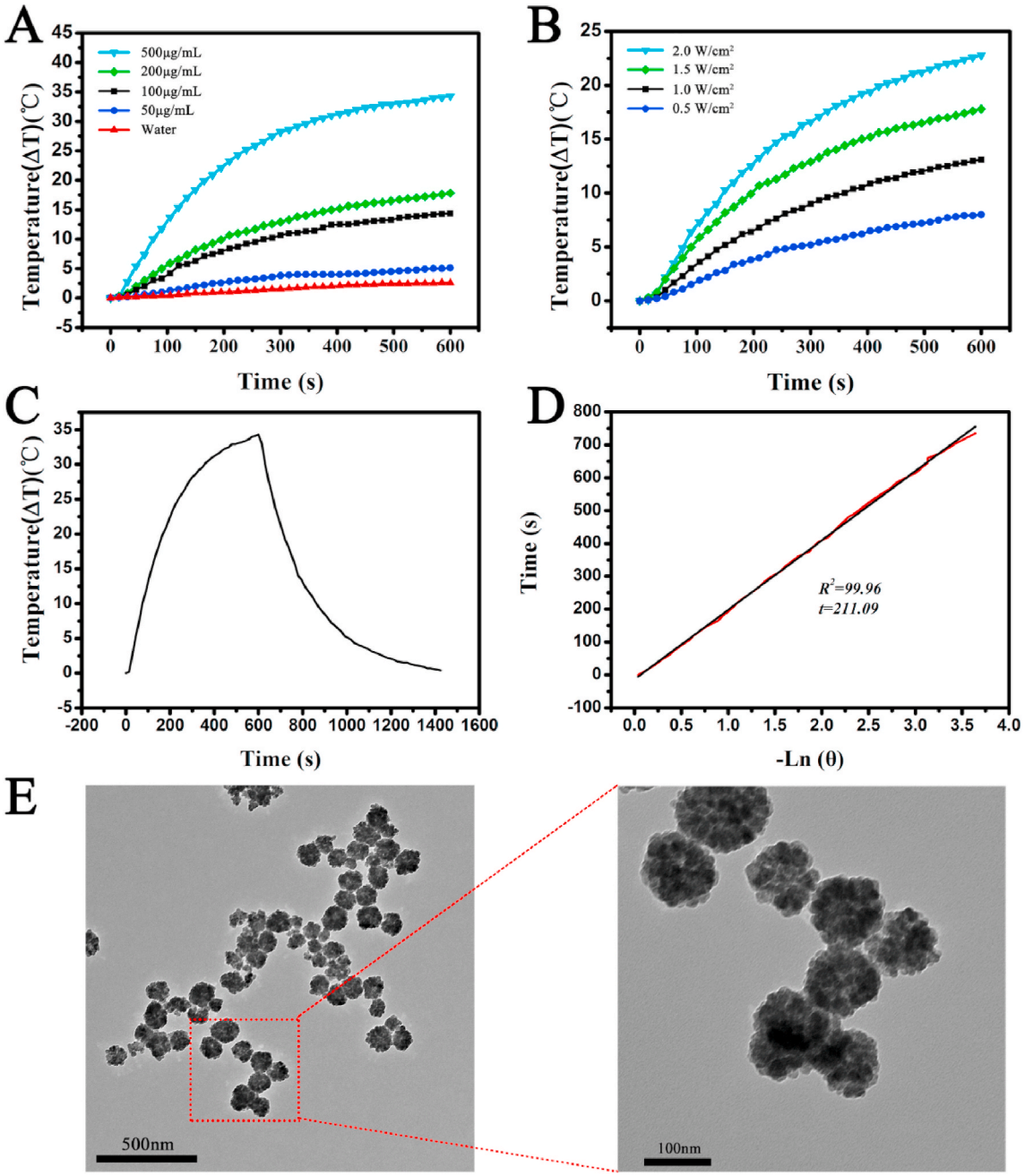

Fig. 2. (A) Temperature curves of EGaIn-Au NPs solution under different concentrations exposed to the 808 nm laser irradiation (1.5 W/cm^2). (B) Photothermal temperature curves of EGaIn-Au NPs at different power densities (0.5 W/cm^2, 1.0 W/cm^2, 1.5 W/cm^2, 2.0 W/cm^2) under 808 nm laser irradiation with the concentration of 200 μg/mL for 10 min. (C) The time constant of EGaIn-Au NPs for heat transfer of system. (D) Curves of cooling time of EGaIn-Au NPs versus negative natural logarithm of the temperature driving force obtained from the cooling stage. (E) TEM images of EGaIn-Au NPs after photothermal heating cycle. Scale bars: 200 nm.

NPs. Five groups of BALB/c mice bearing 4T1 tumor were received different treatment including: (a) i.v. injection of PBS solution (PBS group) (b) i.v. injection of EGaIn-Au NPs solution (EGaIn-Au group, 200 μL, 3 mg/mL) (c) i.v. injection of EGaIn-Au NPs solution +808 nm laser irradiation (EGaIn-Au + NIR group) (d) i.v. injection of EGaIn-Au NPs solution + X-ray (EGaIn-Au + Ray group) (e) i.v. injection of EGaIn-Au NPs solution + X-ray + 808 nm laser irradiation (EGaIn-Au + Ray + NIR group). In EGaIn-Au + Ray + NIR group, 24 h post-injection, the mice were first treated with 6 Gy X-ray irradiation and subsequently processed by 808 nm laser exposure for 10 min. As shown in Fig. 5A, the local temperature of tumor tissue upon NIR exposure could increase about 24.2 ˚C, much higher than that of control group. The *in vivo* investigation lasted for 19 days and during this process the relative body weight in all groups were not obviously affected, demonstrating its excellent biocompatibility and low toxicity without acute side effects (Fig. 5B). In order to investigate the *in vivo* biodistribution features of EGaIn-Au NPs on the BALB/c mice and study the body clearance of NPs, the amounts of the EGaIn-Au NPs accumulated in the vital organs (liver and kidney) were tested by inductively coupled plasma-optical emission spectroscopy (ICP-OES) measurements at various time points (0, 1, 3, 7 day). Fig. 5C revealed that the EGaIn-Au NPs had a high concentration of Ga in liver and kidney at 24 h post-injection, and then were cleared from body on day 3. The tumor size measurement was performed every 2 days using avernier caliper. Tumor

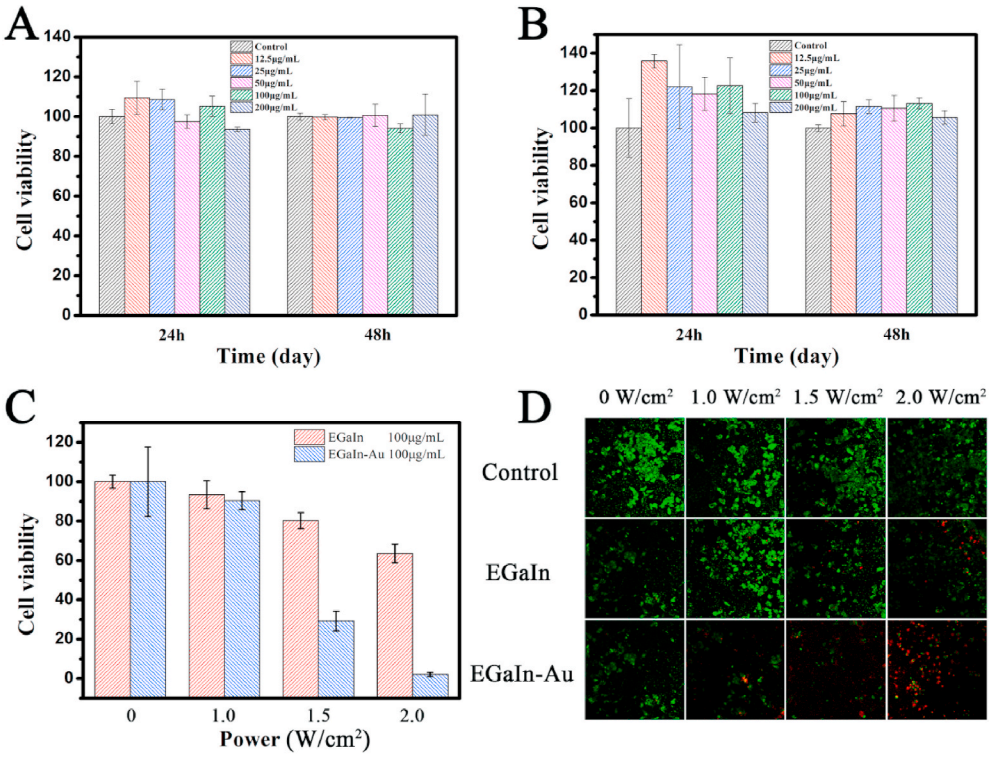

Fig. 3. (A) *In vitro* cell viability of L929 cells incubated with different concentrations of EGaIn NPs and (B) EGaIn-Au NPs for 24, 48 h respectively. (C) Cell viability of 4T1 cells under different treatments. (D) Fluorescence images of 4T1 cells stained with Calcein-AM/PI for live/dead test with and without the addition of EGaIn and EGaIn-Au NPs (100 μg/mL) after 808 nm laser irradiation with 1.0, 1.5, 2.0 W/cm^2 power density for 5 min.

volume was calculated according to the formulation: V = width^2 × length/2, and the relative volume was also calculated. It could be noticed in Fig. 5D–F, single treatment by either photothermal therapy or X-ray irradiation therapy could only inhibit the growth of tumor as compared with the control group. However, a significant therapeutic effect could be observed in EGaIn-Au + Ray + NIR group, indicating the combination of X-ray irradiation therapy and photothermal therapy mediated by EGaIn-Au NPs could greatly enhance the antitumor effect. After 19 days, the mice were sacrificed. Meanwhile, tumor tissues and major organs (heart, liver, spleen, lung, kidney) were collected for preparation of histological section. It could be noticed that the combination of photothermal therapy and radiotherapy induced by EGaIn-Au NPs could effectively lead to the severe necrosis phenomenon for tumor cells (Fig. 5G–K). More importantly, there were no obvious tissue damage could be found in major organs (Fig. 6). Finally, the *in vivo* long-term toxicity/safety of EGaIn-Au NPs was investigated in healthy BALB/c mice. The mice were divided into four groups (N = 5) and administered intravenously with EGaIn-Au NPs at different dose 30 mg kg^{-1}, 60 mg kg^{-1}, 90 mg kg^{-1} and 120 mg kg^{-1}. During the treatment of 2 weeks, the mice in all groups were at stable growth without obvious difference in treatment groups (Fig. S5), indicating that the EGaIn-Au NPs possessed high biocompatibility and biosafety.

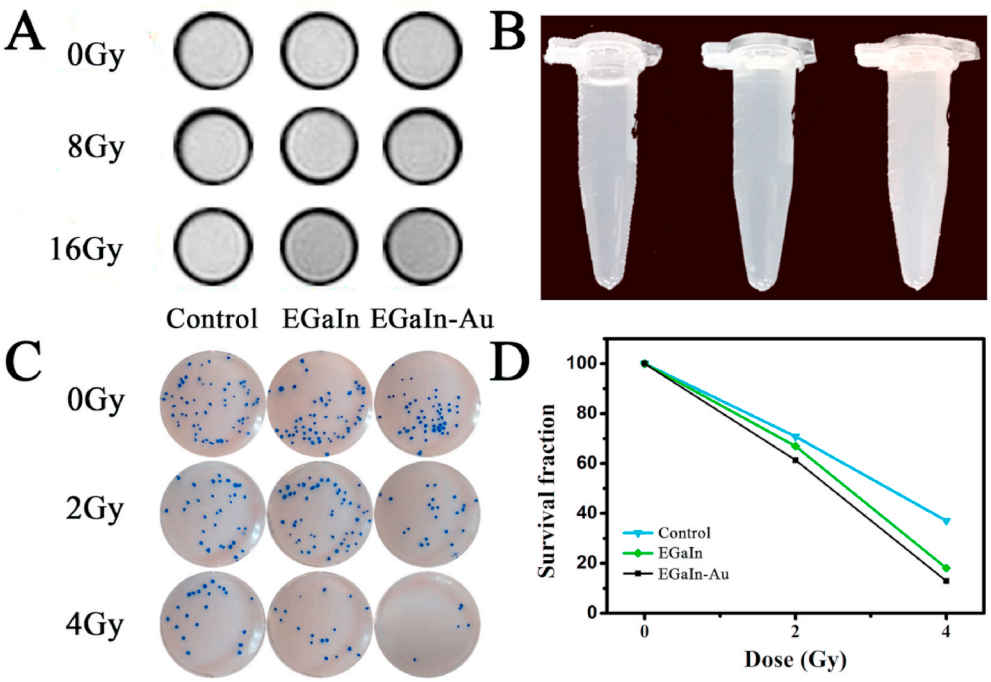

Fig. 4. Gel dosimetry and clonogenic assay (A) T_2 MR image of gels with different treatments under 0 Gy, 8 Gy, 16 Gy X-ray radiation dose. (B) The color change of gel under 8 Gy with 100 μg/mL material: control group (left), EGaIn group (middle) and EGaIn-Au group (right). (C, D) Photographs of colony formation assay of 4T1 cells in control group (left), GaIn NPs group (middle) and EGaIn-Au NPs group under 0 Gy, 2 Gy, 4 Gy X-ray radiation dose and corresponding survival fraction.

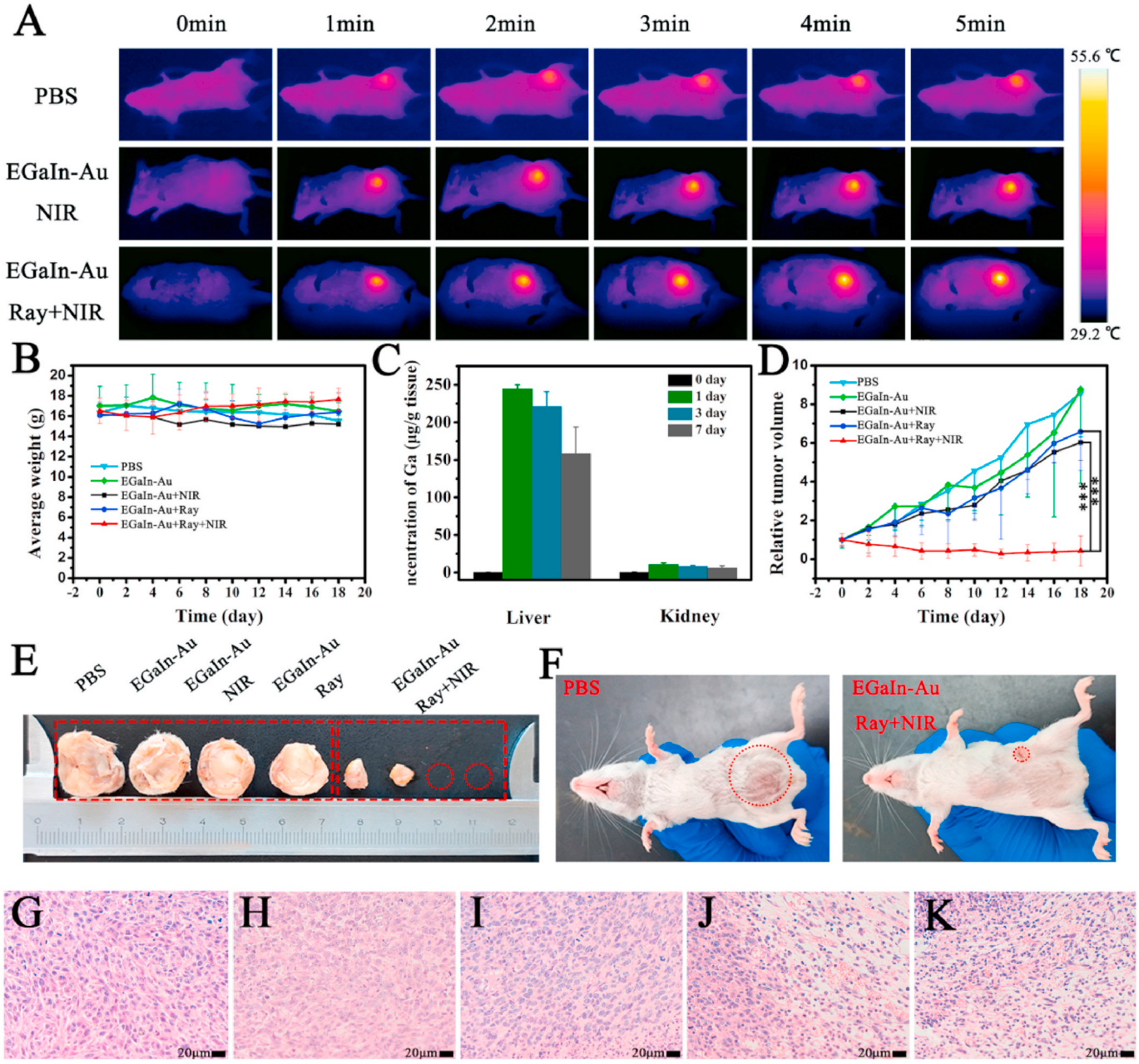

Fig. 5. (A) IR thermal images of tumor-bearing mice for showing the rising temperature of tumor tissue region against the 808 nm laser irradiation at 1.5 W/cm^2 for 5 min after PBS, EGaIn + NIR, EGaIn-Au + Ray + NIR treatment. (B, D) Quantitative measurement and calculation of tumor volume and body weight of mice after various treatment including PBS group (cyan), EGaIn-Au group (green), EGaIn-Au + NIR group (black), EGaIn-Au + Ray group (blue), EGaIn-Au + Ray + NIR group (red). (C) Biodistribution of Ga accumulation in liver and kidney organs of BALB/c mice after treatment with EGaIn-Au NPs at 0, 1, 3, 7 day postinjection measured by inductively coupled plasma-optical emission spectroscopy, Error bars indicate standard deviations, N = 3. (100 μL, 3 mg kg^{-1}) (**P < 0.01, ***P < 0.001) (E) Typical tumor tissue under different treatments after 19 days. (F) Typical mice under PBS and EGaIn-Au + Ray + NIR treatment after 19 days. (G–K) Histology staining of tumor tissue slices obtained from mice with various treatments (PBS, EGaIn-Au, EGaIn-Au + NIR, EGaIn-Au + Ray, EGaIn-Au + Ray + NIR) after 19 days. Scale bar: 20 μm.

4. Conclusions

In current work, we have successfully fabricated the litchi-shaped EGaIn-Au nano-composite based on in situ interfacial galvanic replacement reaction between EGaIn NPs and Au ions. The uniform distribution of Ga, In, Au element on the surface of EGaIn-Au NPs can be obviously presented by EDS spectrum. Moreover, benefiting from the increase in surface area and the excellent stabilization effect of xanthan gum, the EGaIn NPs showed ideal photo-induced heat ability. The embedding of Au NPs onto the surface of EGaIn NPs could significantly enhance the photothermal conversion ability to amplify hyperthermia ablation against tumor cells. Furthermore, Au NPs could also increase the radiation sensitivity of EGaIn NPs, which was confirmed by gel dosimetry and clonogenic assay test. In term of these multifunctional properties, the EGaIn-Au nano-composite exhibited an obviously improved tumor growth inhibition under the combination of photothermal therapy and irradiation therapy, indicating its potential application for tumor therapy as functional agent. Finally, we thus believed that the construction of composites via in situ interfacial galvanic replacement reaction based on nano-LM can be potentially extended to the systems of other materials so as to obtain new materials with advanced multi-functionalities.

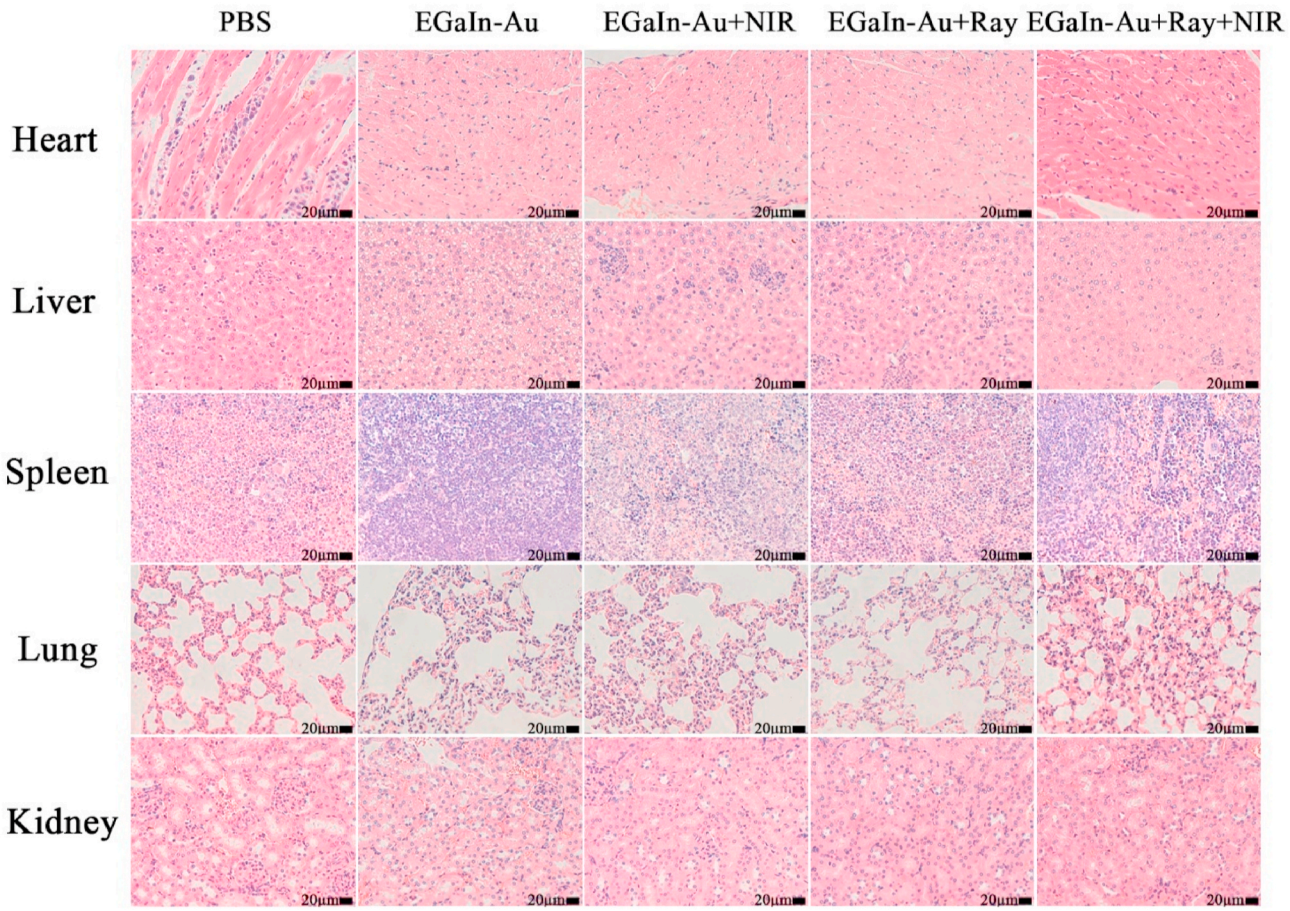

Fig. 6. Hematoxylin-eosin (HE) staining histological images of major organs including heart, liver, spleen, lung, kidney after treatment with PBS, EGaIn-Au, EGaIn-Au + NIR, EGaIn-Au + Ray, EGaIn-Au + Ray + NIR. Scale bar: 20 μm.

Author contributions

Lingyun. Zhao conceived and directed the research project. Zhenhu Guo and Dan Wang prepared and characterized the nano-composites. Zhenhu Guo and Yongjie Chi tested the detailed photothermal properties of two samples. Zhenhu Guo and Jingsong Lu carried out the *in vitro* cell experiment including *in vitro* biocompatibility and cytotoxicity in L929 cells and 4T1 cells respectively. Zhenhu Guo, Dan Wang and Wensheng Xie designed gel dosimetry and clonogenic assay to evaluate radiosensitization effect. Zhenhu Guo and Jingsong Lu performed the animal experiments to estimate *in vivo* anticancer efficiency. Jianzhong Xu, Nonaka Takuya, Junxin Zhang, Wanling Xu, Fei Gao and Zhenhu Guo analyzed the experimental results. Zhenhu Guo, Hong Wu and Lingyun Zhao wrote the paper. All authors approve the final version of the manuscript.

CRediT authorship contribution statement

Zhenhu Guo: Data curation, Formal analysis, Investigation, Methodology, Software, Validation, Writing - original draft, Writing - review & editing. **Jingsong Lu:** Formal analysis, Investigation, Methodology, Software. **Dan Wang:** Investigation, Methodology. **Wensheng Xie:** Investigation, Methodology. **Yongjie Chi:** Formal analysis, Investigation. **Nonaka Takuya:** Formal analysis, Investigation. **Junxin Zhang:** Formal analysis, Investigation. **Wanling Xu:** Formal analysis, Investigation. **Fei Gao:** Formal analysis, Investigation, Methodology. **Hong Wu:** Conceptualization, Writing - original draft, Writing - review & editing. **Lingyun Zhao:** Conceptualization, Formal analysis, Funding acquisition, Supervision, Writing - original draft, Writing - review & editing.

Declaration of competing interest

The authors declare no conflict of interest.

Acknowledgements

This study was supported by grants of the National Natural Science Foundation of China (Nos. 5197116, 81671829).

Appendix A. Supplementary data

Supplementary data to this article can be found online at https://doi.org/10.1016/j.bioactmat.2020.08.033.

References

[1] Q. Wang, Y. Yu, J. Liu, Preparations, characteristics and applications of the functional liquid metal materials, Adv. Eng. Mater. 20 (5) (2018) 1700781, , https://doi.org/10.1002/adem.201700781.
[2] J. Yan, Y. Lu, G. Chen, M. Yang, Z. Gu, Advances in liquid metals for biomedical applications, Chem. Soc. Rev. 47 (8) (2018) 2518–2533, https://doi.org/10.1039/c7cs00309a.

[3] M. Zhang, S. Yao, W. Rao, J. Liu, Transformable soft liquid metal micro/nanomaterials, Mater. Sci. Eng. R Rep. 138 (2019) 1–35, https://doi.org/10.1016/j.mser.2019.03.001.

[4] A. Pandey, S. Kulkarni, S. Mutalik, Liquid metal based theranostic nanoplatforms: application in cancer therapy, imaging and biosensing, Nanomed. Nanotechnol. Biol. Med. 26 (2020) 102175, , https://doi.org/10.1016/j.nano.2020.102175.

[5] L. Yi, J. Liu, Liquid metal biomaterials: a newly emerging area to tackle modern biomedical challenges, Int. Mater. Rev. 62 (7) (2017) 415–440, https://doi.org/10.1080/09506608.2016.1271090.

[6] X. Zhao, G. Li, Y. Li, H. X, Magnetoacoustic signal analysis of bio-tissue containing liquid metal, J. Phys. D Appl. Phys. 53 (6) (2020) 065401, , https://doi.org/10.1088/1361-6463/ab56a4.

[7] Q. Wang, Y. Yu, K. Pan, J. Liu, Liquid metal angiography for mega contrast X-ray visualization of vascular network in reconstructing in-vitro organ anatomy, IEEE Trans. Biomed. Eng. 61 (7) (2014) 2161–2166, https://doi.org/10.1109/TBME.2014.2317554.

[8] L. Yi, C. Jin, L. Wang, J. Liu, Liquid-solid phase transition alloy as reversible and rapid molding bone cement, Biomaterials 35 (37) (2014) 9789–9801, https://doi.org/10.1016/j.biomaterials.2014.08.048.

[9] Y. Lu, Q. Hu, Y. Lin, D.B. Pacardo, C. Wang, W. Sun, F.S. Ligler, M.D. Dickey, Z. Gu, Transformable liquid-metal nanomedicine, Nat. Commun. 6 (2015) 10066, https://doi.org/10.1038/ncomms10066.

[10] Y. Lu, Y. Lin, Z. Chen, Q. Hu, Y. Liu, S. Yu, W. Gao, M.D. Dickey, Z. Gu, Enhanced endosomal escape by light-fueled liquid-metal transformer, Nano Lett. 17 (4) (2017) 2138–2145, https://doi.org/10.1021/acs.nanolett.6b04346.

[11] D. Kim, J. Hwang, Y. Choi, Y. Kwon, J. Jang, S. Yoon, J. Choi, Effective delivery of anti-cancer drug molecules with shape transforming liquid metal particles, Cancers 11 (11) (2019) 1666, https://doi.org/10.3390/cancers11111666.

[12] X. Wang, L. Fan, J. Zhang, X. Sun, H. Chang, B. Yuan, R. Guo, M. Duan, J. Liu, Printed conformable liquid metal e-skin-enabled spatiotemporally controlled bioelectromagnetics for wireless multisite tumor therapy, Adv. Funct. Mater. 29 (51) (2019) 1907063, , https://doi.org/10.1002/adfm.201907063.

[13] D. Wang, W. Xie, Q. Gao, H. Yan, J. Zhang, J. Lu, B. Liaw, Z. Guo, F. Gao, L. Yin, G. Zhang, L. Zhao, Non-magnetic injectable implant for magnetic field-driven thermochemotherapy and dual stimuli-responsive drug delivery: transformable liquid metal hybrid platform for cancer theranostics, Small 15 (16) (2019) 1900511, , https://doi.org/10.1002/smll.201900511.

[14] J. Hu, M. Liu, Y. Chen, F. Gao, S. Peng, B. Xie, C. Li, X. Zeng, X. Zhang, Immobilized liquid metal nanoparticles with improved stability and photothermal performance for combinational therapy of tumor, Biomaterials 207 (2019) 76–88, https://doi.org/10.1016/j.biomaterials.2019.03.043.

[15] N. Xia, N. Li, W. Rao, J. Yu, Q. Wu, L. Tan, H. Li, L. Gou, P. Liang, L. Li, X. Meng, Multifunctional and flexible ZrO_2-coated EGaIn nanoparticles for photothermal therapy, Nanoscale 11 (21) (2019) 10183–10189, https://doi.org/10.1039/c9nr01963d.

[16] X. Wang, W. Yao, R. Guo, X. Yang, J. Tang, J. Zhang, W. Gao, V. Timchenko, J. Liu, Soft and moldable Mg-doped liquid metal for conformable skin tumor photothermal therapy, Adv Healthc Mate 7 (14) (2018) 1800318, , https://doi.org/10.1002/adhm.201800318.

[17] L. Fan, M. Duan, Z. Xie, K. Pan, X. Wang, X. Sun, Q. Wang, W. Rao, J. Liu, Injectable and radiopaque liquid metal/calcium alginate hydrogels for endovascular embolization and tumor embolotherapy, Small 16 (2) (2020) 1903421, , https://doi.org/10.1002/smll.201903421.

[18] Q. Wu, N. Xia, D. Long, L. Tan, W. Rao, J. Yu, C. Fu, X. Ren, H. Li, L. Gou, P. Liang, J. Ren, L. Li, X. Meng, Dual-functional supernanoparticles with microwave dynamic therapy and microwave thermal therapy, Nano Lett. 19 (8) (2019) 5277–5286, https://doi.org/10.1021/acs.nanolett.9b01735.

[19] F. Hoshyargar, J. Crawford, A.P. O'Mullane, Galvanic replacement of the liquid metal galinstan, J. Am. Chem. Soc. 139 (4) (2017) 1464–1471, https://doi.org/10.1021/jacs.6b05957.

[20] T. Daeneke, K. Khoshmanesh, N. Mahmood, I.A. de Castro, D. Esrafilzadeh, S.J. Barrow, M.D. Dickey, K. Kalantar-Zadeh, Liquid metals: fundamentals and applications in chemistry, Chem. Soc. Rev. 47 (11) (2018) 4073–4111, https://doi.org/10.1039/c7cs00043j.

[21] A. Martin, W. Kiarie, B. Chang, M. Thuo, Chameleon metals: autonomous nanotexturing and composition inversion on liquid metals surfaces, Angew. Chem. Int. Ed. 59 (1) (2020) 352–357, https://doi.org/10.1002/anie.201912639.

[22] S.-Y. Tang, R. Qiao, S. Yan, D. Yuan, Q. Zhao, G. Yun, T.P. Davis, W. Li, Microfluidic mass production of stabilized and stealthy liquid metal nanoparticles, Small 14 (21) (2018) 1800118, , https://doi.org/10.1002/smll.201800118.

[23] R. Guo, J. Tang, S. Dong, J. Lin, H. Wang, J. Liu, W. Rao, One-step liquid metal transfer printing: toward fabrication of flexible electronics on wide range of substrates, Adv Mater Technol 3 (12) (2018) 1800265, https://doi.org/10.1002/admt.201800265.

[24] A. Zavabeti, J.Z. Ou, B.J. Carey, N. Syed, R. Orrell-Trigg, E.L.H. Mayes, C. Xu, O. Kavehei, A.P. O'Mullane, R.B. Kaner, K. Kalantar-zadeh, T. Daeneke, A liquid metal reaction environment for the room-temperature synthesis of atomically thin metal oxides, Science 358 (6361) (2017) 332–335, https://doi.org/10.1126/science.aao4249.

[25] V. Sivan, S.-Y. Tang, A.P. O'Mullane, P. Petersen, N. Eshtiaghi, K. Kalantar-zadeh, A. Mitchell, Liquid metal marbles, Adv. Funct. Mater. 23 (2) (2013) 144–152, https://doi.org/10.1002/adfm.201200837.

[26] H. Song, T. Kim, S. Kang, H. Jin, K. Lee, H.J. Yoon, Ga-based liquid metal micro/nanoparticles: recent advances and applications, Small 16 (12) (2019) e1903391, , https://doi.org/10.1002/smll.201903391.

[27] S.Y. Tang, B. Ayan, N. Nama, Y. Bian, J.P. Lata, X. Guo, T.J. Huang, On-chip production of size-controllable liquid metal microdroplets using acoustic waves, Small 12 (28) (2016) 3861–3869, https://doi.org/10.1002/smll.201600737.

[28] A. Yamaguchi, Y. Mashima, T. Iyoda, Reversible size control of liquid-metal nanoparticles under ultrasonication, Angew. Chem. Int. Ed. 54 (43) (2015) 12809–12813, https://doi.org/10.1002/anie.201506469.

[29] S.A. Chechetka, Y. Yu, X. Zhen, M. Pramanik, K. Pu, E. Miyako, Light-driven liquid metal nanotransformers for biomedical theranostics, Nat. Commun. 8 (2017) 15432, https://doi.org/10.1038/ncomms15432.

[30] J.J. Hu, M.D. Liu, F. Gao, Y. Chen, S.Y. Peng, Z.H. Li, H. Cheng, X.Z. Zhang, Photocontrolled liquid metal nanoparticle-enzyme for starvation/photothermal therapy of tumor by win-win cooperation, Biomaterials 217 (2019) 119303, , https://doi.org/10.1016/j.biomaterials.2019.119303.

[31] A. Elbourne, S. Cheeseman, P. Atkin, N.P. Truong, N. Syed, A. Zavabeti, M. Mohiuddin, D. Esrafilzadeh, D. Cozzolino, C.F. McConville, M.D. Dickey, R.J. Crawford, K. Kalantar-Zadeh, J. Chapman, T. Daeneke, V.K. Truong, Antibacterial liquid metals: biofilm treatment via magnetic activation, ACS Nano 14 (1) (2020) 802–817, https://doi.org/10.1021/acsnano.9b07861.

[32] C. Pan, E.J. Markvicka, M.H. Malakooti, J. Yan, L. Hu, K. Matyjaszewski, C. Majidi, A liquid-metal-elastomer nanocomposite for stretchable dielectric materials, Adv. Mater. 31 (23) (2019) e1900663, , https://doi.org/10.1002/adma.201900663.

[33] S. Mei, Y. Gao, Z. Deng, J. Liu, Thermally conductive and highly electrically resistive grease through homogeneously dispersing liquid metal droplets inside methyl silicone oil, J. Electron. Packag. 136 (1) (2014) 011009, , https://doi.org/10.1115/1.4026414.

[34] R. Zheng, Z. Peng, Y. Fu, Z. Deng, S. Liu, S. Xing, Y. Wu, J. Li, L. Liu, A novel conductive core–shell particle based on liquid metal for fabricating real-time self-repairing flexible circuits, Adv. Funct. Mater. 30 (15) (2020) 1910524, , https://doi.org/10.1002/adfm.201910524.

[35] M.B. Ghasemian, M. Mayyas, S.A. Idrus-Saidi, M.A. Jamal, J. Yang, S.S. Mofarah, E. Adabifiroozjaei, J. Tang, N. Syed, A.P. O'Mullane, T. Daeneke, K. Kalantar-Zadeh, Self-limiting galvanic growth of MnO_2 monolayers on a liquid metal—applied to photocatalysis, Adv. Funct. Mater. 29 (36) (2019) 1901649, , https://doi.org/10.1002/adfm.201901649.

[36] E. Boisselier, D. Astruc, Gold nanoparticles in nanomedicine: preparations, imaging, diagnostics, therapies and toxicity, Chem. Soc. Rev. 38 (6) (2009) 1759–1782, https://doi.org/10.1039/b806051g.

[37] Y. Cheng, Y. Chang, Y. Feng, H. Jian, Z. Tang, H. Zhang, Deep-level defect enhanced photothermal performance of bismuth sulfide-gold heterojunction nanorods for photothermal therapy of cancer guided by computed tomography imaging, Angew. Chem. Int. Ed. 57 (1) (2018) 246–251, https://doi.org/10.1002/anie.201710399.

[38] J. Chen, X. Li, X. Zhao, Q. Wu, H. Zhu, Z. Mao, C. Gao, Doxorubicin-conjugated pH-responsive gold nanorods for combined photothermal therapy and chemotherapy of cancer, Bioact Mater 3 (3) (2018) 347–354, https://doi.org/10.1016/j.bioactmat.2018.05.003.

[39] S. Zhang, W. Guo, J. Wei, C. Li, X.J. Liang, M. Yin, Terrylenediimide-based intrinsic theranostic nanomedicines with high photothermal conversion efficiency for photoacoustic imaging-guided cancer therapy, ACS Nano 11 (4) (2017) 3797–3805, https://doi.org/10.1021/acsnano.6b08720.

[40] D.K. Roper, W. Ahn, M. Hoepfner, Microscale heat transfer transduced by surface plasmon resonant gold nanoparticles, J. Phys. Chem. C 111 (9) (2007) 3636–3641, https://doi.org/10.1021/jp064341w.

[41] M.F. Peter, C.K. Derek, D.D. Mark, C.G. John, Polymer gels for magnetic resonance imaging of radiation dose distributions at normal room atmosphere, Phys. Med. Biol. 46 (12) (2001) 3105, https://doi.org/10.1088/0031-9155/46/12/303.

[42] A. Rajaee, L. Zhao, S. Wang, D. Wang, Y. Liu, J. Wang, K. Ying, Multifunction bismuth gadolinium oxide nanoparticles as radiosensitizer in radiation therapy and imaging, Phys. Med. Biol. 64 (19) (2019) 195007, , https://doi.org/10.1088/1361-6560/ab2154.

[43] A. Palaniraj, V. Jayaraman, Production, recovery and applications of xanthan gum by Xanthomonas campestris, J. Food Eng. 106 (1) (2011) 1–12, https://doi.org/10.1016/j.jfoodeng.2011.03.035.

[44] F. Garcia-Ochoa, V.E. Santos, J.A. Casas, E. Gomez, Xanthan gum: production, recovery, and properties, Biotechnol. Adv. 18 (7) (2000) 549–579, https://doi.org/10.1016/S0734-9750(00)00050-1.

[45] H. Wang, B. Yuan, S. Liang, R. Guo, W. Rao, X. Wang, H. Chang, Y. Ding, J. Liu, L. Wang, PLUS-M: a porous liquid-metal enabled ubiquitous soft material, Mater Horiz 5 (2) (2018) 222–229, https://doi.org/10.1039/c7mh00989e.

[46] Y. Cui, F. Liang, C. Ji, S. Xu, H. Wang, Z. Lin, J. Liu, Discoloration effect and one-step synthesis of hydrogen tungsten and molybdenum bronze ($HxMO_3$) using liquid metal at room temperature, ACS Omega 4 (4) (2019) 7428–7435, https://doi.org/10.1021/acsomega.9b00840.

[47] S. Liang, W. Rao, K. Song, J. Liu, Fluorescent liquid metal as a transformable biomimetic chameleon, ACS Appl. Mater. Interfaces 10 (2) (2018) 1589–1596, https://doi.org/10.1021/acsami.7b17233.

[48] X. Sun, B. Yuan, W. Rao, J. Liu, Amorphous liquid metal electrodes enabled conformable electrochemical therapy of tumors, Biomaterials 146 (2017) 156–167, https://doi.org/10.1016/j.biomaterials.2017.09.006.

[49] D. Jaque, L. Maestro, M.B. Rosal, del P. Haro-Gonzalez, A. Benayas, J. Plaza, L.E. Rodríguez, M.J. Solé G, Nanoparticles for photothermal therapies, Nanoscale 6 (16) (2014) 9494–9530, https://doi.org/10.1039/c4nr00708e.

[50] Y. Liu, P. Bhattarai, Z. Dai, X. Chen, Photothermal therapy and photoacoustic imaging via nanotheranostics in fighting cancer, Chem. Soc. Rev. 48 (7) (2019) 2053–2108, https://doi.org/10.1039/c8cs00618k.

[51] Y. Lin, Y. Liu, J. Genzer, M.D. Dickey, Shape-transformable liquid metal

nanoparticles in aqueous solution, Chem. Sci. 8 (5) (2017) 3832–3837, https://doi.org/10.1039/c7sc00057j.
[52] C.C. Huang, C.S. Yeh, Laser ablation synthesis of spindle-like gallium oxide hydroxide nanoparticles with the presence of cationic cetyltrimethylammonium bromide, J. Phys. Chem. B 108 (16) (2004) 4940–4945, https://doi.org/10.1021/jp037427n.
[53] Q. Chen, J. Chen, Z. Yang, J. Xu, L. Xu, C. Liang, X. Han, Z. Liu, Nanoparticle-enhanced radiotherapy to trigger robust cancer immunotherapy, Adv. Mater. 31 (10) (2019) e1802228, , https://doi.org/10.1002/adma.201802228.
[54] S. Shi, R. Vissapragada, J. Abi Jaoude, C. Huang, A. Mittal, E. Liu, J. Zhong, V. Kumar, Evolving role of biomaterials in diagnostic and therapeutic radiation oncology, Bioact Mater 5 (2) (2020) 233–240, https://doi.org/10.1016/j.bioactmat.2020.01.011.
[55] P.M. Fong, D.C. Keil, M.D. Does, J.C. Gore, Polymer gels for magnetic resonance imaging of radiation dose distributions at normal room atmosphere, Phys. Med. Biol. 46 (12) (2001) 3105–3113, https://doi.org/10.1088/0031-9155/46/12/303.